Quantitative confocal phase imaging by synthetic optical holography

M. Schnell,[1] M. J. Perez-Roldan,[1] P. S. Carney,[2,5] and R. Hillenbrand[3,4,*]

[1]*CIC nanoGUNE, 20018 Donostia – San Sebastian, Spain*
[2]*Department Electrical and Computer Engineering and The Beckman Institute for Advanced Science and Technology, University of Illinois, Urbana, Illinois 61801, USA*
[3]*CIC nanoGUNE and UPV/EHU, 20018 Donostia – San Sebastian, Spain*
[4]*IKERBASQUE, Basque Foundation for Science, 48011 Bilbao, Spain*
[5]*carney@uiuc.edu*
[*]*r.hillenbrand@nanogune.eu*

Abstract: We demonstrate quantitative phase mapping in confocal optical microscopy by applying synthetic optical holography (SOH), a recently introduced method for technically simple and fast phase imaging in scanning optical microscopy. SOH is implemented in a confocal microscope by simply adding a linearly moving reference mirror to the microscope setup, which generates a synthetic reference wave analogous to the plane reference wave of wide-field off-axis holography. We demonstrate that SOH confocal microscopy allows for non-contact surface profiling with sub-nanometer depth resolution. As an application for biological imaging, we apply SOH confocal microscopy to map the surface profile of an onion cell, revealing nanoscale-height features on the cell surface.

OCIS codes: (090.0090) Holography; (120.3940) Metrology; (180.1790) Confocal microscopy.

References and links

1. R. H. Webb, "Confocal optical microscopy," Rep. Prog. Phys. **59**(3), 427–471 (1996).
2. T. Wilson, *Confocal Microscopy* (Academic, 1990).
3. D. J. Whitehouse, *Handbook of Surface and Nanometrology* (CRC Press, 2011).
4. W. Osten, *Optical Inspection of Microsystems* (CRC Press, 2007).
5. G. E. Sommargren, "Optical heterodyne profilometry," Appl. Opt. **20**(4), 610–618 (1981).
6. D. Pantzer, J. Politch, and L. Ek, "Heterodyne profiling instrument for the angstrom region," Appl. Opt. **25**(22), 4168–4172 (1986).
7. T. Sawatari, "Optical heterodyne scanning microscope," Appl. Opt. **12**(11), 2768–2772 (1973).
8. A. Mitra, B. Deutsch, F. Ignatovich, C. Dykes, and L. Novotny, "Nano-optofluidic detection of single viruses and nanoparticles," ACS Nano **4**(3), 1305–1312 (2010).
9. H. J. Matthews, D. K. Hamilton, and C. J. R. Sheppard, "Surface profiling by phase-locked interferometry," Appl. Opt. **25**(14), 2372–2374 (1986).
10. B. Deutsch, R. Beams, and L. Novotny, "Nanoparticle detection using dual-phase interferometry," Appl. Opt. **49**(26), 4921–4925 (2010).
11. J. E. Graebner, B. P. Barber, P. L. Gammel, D. S. Greywall, and S. Gopani, "Dynamic visualization of subangstrom high-frequency surface vibrations," Appl. Phys. Lett. **78**(2), 159–161 (2001).
12. J. V. Knuuttila, P. T. Tikka, and M. M. Salomaa, "Scanning Michelson interferometer for imaging surface acoustic wave fields," Opt. Lett. **25**(9), 613–615 (2000).
13. S. Lai, R. A. McLeod, P. Jacquemin, S. Atalick, and R. Herring, "An algorithm for 3-D refractive index measurement in holographic confocal microscopy," Ultramicroscopy **107**(2-3), 196–201 (2007).
14. A. S. Goy and D. Psaltis, "Digital confocal microscope," Opt. Express **20**(20), 22720–22727 (2012).
15. R. A. Herring, "Confocal scanning laser holography, and an associated microscope: a proposal," Optik **105**, 65–68 (1997).
16. M. Schnell, P. S. Carney, and R. Hillenbrand, "Synthetic optical holography for rapid nanoimaging," Nat. Commun. **5**, 3499 (2014).
17. R. Wen, A. Lahiri, M. Azhagurajan, S.-i. Kobayashi, and K. Itaya, "A new in situ optical microscope with single atomic layer resolution for observation of electrochemical dissolution of Au(111)," J. Am. Chem. Soc. **132**(39), 13657–13659 (2010).
18. D. Parshall and M. K. Kim, "Digital holographic microscopy with dual-wavelength phase unwrapping," Appl. Opt. **45**(3), 451–459 (2006).
19. M. G. Somekh, M. S. Valera, and R. K. Appel, "Scanning heterodyne confocal differential phase and intensity microscope," Appl. Opt. **34**(22), 4857–4868 (1995).

#209297 - $15.00 USD Received 31 Mar 2014; revised 28 May 2014; accepted 31 May 2014; published 13 Jun 2014

20. N. Warnasooriya and M. K. Kim, "LED-based multi-wavelength phase imaging interference microscopy," Opt. Express **15**(15), 9239–9247 (2007).
21. M. Guillon and M. A. Lauterbach, "Quantitative confocal spiral phase contrast," J. Opt. Soc. Am. A **31**(6), 1215–1225 (2014).
22. T. Sankar, P. M. Delaney, R. W. Ryan, J. Eschbacher, M. Abdelwahab, P. Nakaji, S. W. Coons, A. C. Scheck, K. A. Smith, R. F. Spetzler, and M. C. Preul, "Miniaturized handheld confocal microscopy for neurosurgery: results in an experimental glioblastoma model," Neurosurgery **66**(2), 410–418 (2010).
23. M. Sticker, M. Pircher, E. Götzinger, H. Sattmann, A. F. Fercher, and C. K. Hitzenberger, "En face imaging of single cell layers by differential phase-contrast optical coherence microscopy," Opt. Lett. **27**(13), 1126–1128 (2002).

1. Introduction

Confocal optical microscopy is an established technique in biological imaging and industrial inspection due to its superior contrast and resolution compared to wide-field microscopy and due to its optical sectioning capabilities [1, 2]. Its strong depth discrimination make confocal microscopy attractive for non-contact surface profiling applications where high depth resolution is required, as, for example, in the inspection of microdevices and micoelectromechanical systems (MEMS) [3, 4]. Surface profiling with nanometer-scale depth resolution can be achieved with interferometry techniques which measure the optical phase of the light beam reflected from the sample surface. Interferometric detection has been realized in several modalities such as heterodyne [5–8], phase-locked [9], dual-phase [10] and scanning-interferometer [11, 12] confocal microscopy. The implementation of these modalities, however, is rather complex, requiring dedicated components such as Wollaston prisms, acousto-optical modulators, modulated lasers or rapidly moving mirrors. In alternatives [13–15], holographic instead of interferometric principles where used to detect the optical phase at each pixel individually.

Recently, we introduced synthetic optical holography (SOH) as a new and technically simple holographic modality for quantitative phase imaging in scanning optical microscopy and demonstrated it with a scanning near-field microscope [16]. While scanning the sample, the scattered light from the near-field probe was superposed with a reference field with a linear-in-time phase function. Recording the detector signal pixel-by-pixel produced a near-field image that contained the near-field amplitude and phase information encoded in a fringe pattern reminiscent of a classical hologram. Because of the sequential generation of the reference field, the recorded image was termed a synthetic hologram. Near-field amplitude and phase images could be reconstructed from the synthetic hologram by standard Fourier transform filtering. By taking advantage of the mutual information between the pixels, SOH thus encoded the complex field in a single near-field image with only one datum per pixel in the spirit of wide-field holography.

Here we implement synthetic optical holography (SOH) in confocal optical microscopy. We demonstrate and verify quantitative phase imaging by SOH confocal microscopy in a surface profiling application where we optically measure the topography of a test sample with nanometer-scale depth resolution. We then apply SOH confocal microscopy to map the surface profile of an onion cell, revealing pits and trenches with depths on the 100 nanometer scale and measuring several micrometers in width.

2. Implementation of SOH in a confocal microscope

The implementation of SOH in a confocal microscope is shown in Fig. 1(a). The basis is a homebuilt reflection-mode confocal microscope, where the expanded beam from a stabilized HeNe laser (λ = 632.8 nm) is passed through the beam splitter BS and focused on the sample

#209297 - $15.00 USD Received 31 Mar 2014; revised 28 May 2014; accepted 31 May 2014; published 13 Jun 2014

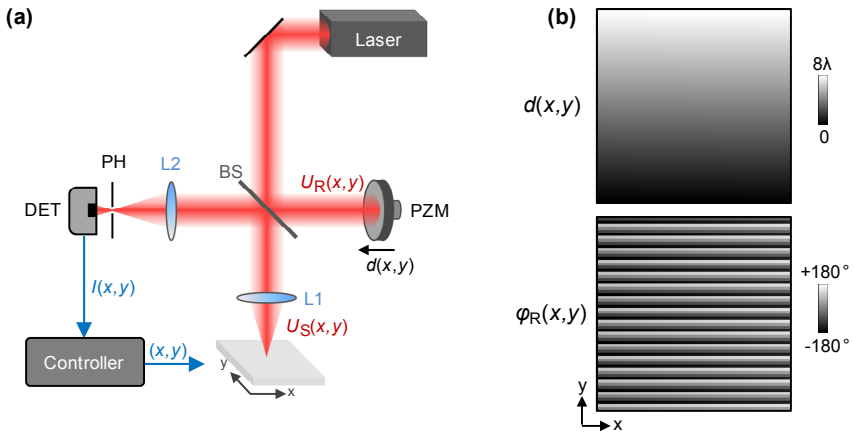

Fig. 1. Implementation of SOH in a confocal microscope. (a) Setup of a SOH confocal microscope. Laser: consisting of a stabilized HeNe laser, Faraday isolator and beam expander, BS: beam-splitter (50:50 non-polarizing), L1: microscope objective (20x, 0.4 NA Nikon E Plan), L2: Lens (f = 25.4mm), PH: pin hole (100 µm diameter for the experiments in Figs. 2 and 3 and 200 µm in case of Fig. 4), PZM: Piezo-actuated mirror, DET: one-pixel photodetector. (b) Linear movement of the reference mirror PZM synthesizes a reference wave $U_R(x,y)$ analogous to the plane reference wave in off-axis wide-field holography. Top: Simulated map of the mirror position $d(x,y)$ consisting of 64 x 64 pixels, where we assumed v_x = 1 mm/s, X = 1 mm, v_R = 1/16 λ/s, Δ_y = 1/64 mm. Bottom: Resulting phase map $\varphi_R(x,y)$ of the synthesized plane reference wave with $k_x = 2\pi/8$ mm^{-1} and $k_y = 16\cdot 2\pi$ mm^{-1}.

surface by the microscope objective L1. The scattered light $U_S(\mathbf{r})$ from the sample is subsequently collected by the microscope objective and focused onto the pinhole PH. At each position $\mathbf{r} = (x, y)$, the scattered light $U_S(\mathbf{r})$ is superposed at the detector with a reference field $U_R(\mathbf{r}) = A_R e^{i\varphi_R(\mathbf{r})}$, which is generated by reflection from the reference mirror PZM. The phase of the reference field $\varphi_R(\mathbf{r}) = 2\pi \cdot 2d(\mathbf{r}) / \lambda$ is controlled by the position $d(\mathbf{r})$ of the reference mirror, which is moved by a linear piezo stage (Physikinstrumente, model P-611). While the sample is rapidly scanned, the reference mirror is slowly translated, yielding a single (quasi-constant) reference phase at each pixel $\mathbf{r}$. Recording the detector signal $I(\mathbf{r})$ pixel-by-pixel, we obtain a synthetic image-plane hologram of the sample,

$$I(\mathbf{r}) = |U_R(\mathbf{r})|^2 + |U_S(\mathbf{r})|^2 + U_S^*(\mathbf{r})U_R(\mathbf{r}) + U_R^*(\mathbf{r})U_S(\mathbf{r}). \qquad (1)$$

By moving the reference mirror PZM at constant velocity v_R, the position of the reference mirror $d(\mathbf{r})$ becomes a function linear in $\mathbf{r}$ and a linear reference wave $U_R(\mathbf{r}) = A_R e^{i\mathbf{k}_\parallel \cdot \mathbf{r}}$ with virtual wave vector $\mathbf{k}_\parallel = (k_x, k_y)$ is synthesized [16],

$$k_x = \frac{4\pi}{\lambda} \cdot \frac{v_R}{v_x} \quad \text{and} \quad k_y = \frac{4\pi}{\lambda} \cdot \frac{v_R}{\Delta_y v_x / 2X}, \qquad (2)$$

where λ is the wavelength of the illuminating beam, v_x the velocity of the sample scanning in the fast scan direction, X the total scan length in the fast scan direction. Δ_y is the step in the slow scan direction taken after completion of each fast scan line, i.e. after completion of a fast forward scan and a subsequent rescan of the same line in backward direction. The synthetic reference wave is analogous to a plane reference wave in off-axis wide-field holography. Exemplarily we show in Fig. 1(b) a simulation of the map of the reference mirror position $d(\mathbf{r})$ and the resulting phase map $\varphi_R(\mathbf{r})$ of the synthesized reference wave. The synthetic

#209297 - $15.00 USD Received 31 Mar 2014; revised 28 May 2014; accepted 31 May 2014; published 13 Jun 2014

image-plane hologram, $I(\mathbf{r})$, can thus be reconstructed using standard Fourier transform (FT) filtering [16],

$$\tilde{I}(\mathbf{q}) = C(\mathbf{q}) + A_R \tilde{U}_S^*\left(\mathbf{k}_\parallel - \mathbf{q}\right) + A_R^* \tilde{U}_S\left(\mathbf{k}_\parallel + \mathbf{q}\right), \tag{3}$$

where the tilde indicates FT with respect to position. $C(\mathbf{q})$ is the autocorrelation term, i.e. the FT of $U_S U_S^*(\mathbf{r}) + A_R^2$. The direct term $A_R^* \tilde{U}_S$ and its conjugate $A_R \tilde{U}_S^*$ are shifted by $-\mathbf{k}_\parallel$ and $\mathbf{k}_\parallel$, respectively. By filtering in FT space, the direct term $A_R^* \tilde{U}_S$ is isolated from the other terms and by subsequent inverse FT, the complex-valued scattered field $U_S(\mathbf{r})$ is recovered. Confocal amplitude and phase images, $A_S(\mathbf{r})$ and $\varphi_S(\mathbf{r})$, can then easily be calculated from $U_S(\mathbf{r})$. Note that in the filtered term $A_R^* \tilde{U}_S$, the recovered field $U_S(\mathbf{r})$ is multiplied by the reference field amplitude A_R. SOH thus not only provides confocal amplitude and phase images, but also an interferometric amplification of the scattered field $U_S(\mathbf{r})$, which can provide a significant signal boost in case of weak scattering.

3. Demonstration of SOH confocal phase imaging with a test sample

We demonstrate and verify holographic confocal amplitude and phase imaging with a phase-only test sample exhibiting pits of different depths. Fabrication of the test sample was performed by focused-ion beam milling on a bare silicon substrate (30kV, 0.46nA). Rectangular pits (10 μm x 8 μm) of different depths were obtained by adjusting the milling time at each pit, yielding a series of pits with depths ranging from 4 to 80 nm (Fig. 2(a)). After milling, the sample was covered by a thin Au film of approx. 40 nm thickness. When imaging the sample with SOH confocal microscopy as described in Fig. 1, the pits introduce changes to the path length of the reflected light beam, thus yielding a defined optical phase contrast with respect to the sample surface. The Au film provides constant reflection amplitude across the whole sample, thus avoiding any additional optical phase changes that might occur as a result of the ion implantation in Si during the milling process. Below, we measure the surface profile from the confocal phase images and compare it against the topography obtained with an atomic force microscope (AFM).

First, we acquired a confocal intensity image by blocking the reference arm of the interferometer (Fig. 2(b)). The same intensity value is observed at all pits because the pit depth is much smaller than the depth resolution of the microscope (approximately 1.2 μm). Thus, the intensity image does not allow to determine the depth of the pits. We note that a dark rim appears at the pit edges, which we attribute to the limited NA of the objective that does not fully capture the reflection of the illuminating beam from the steep pit walls.

Next, we recorded a synthetic hologram by moving the reference mirror at a constant velocity of $v_R = 102.8\,\mathrm{nm/s}$ and by scanning the sample with $v_x = 338\,\mu\mathrm{m/s}$, $X = 130\,\mu\mathrm{m}$ and $\Delta_y = 0.1\,\mu\mathrm{m}$. The velocity v_R is chosen such that reference phase changes by 2π for every 4 lines scanned, which produces a virtual wave vector $\mathbf{k}_\parallel$ of 1/4 of the total image bandwidth, mainly pointing in the y-direction. More precisely, the virtual wave vector is $\mathbf{k}_\parallel = \left(6\cdot 10^{-5}, 1.581\right)\cdot k_0$ where $k_0 = 2\pi/\lambda$ is the free-space wavenumber. The synthetic hologram, $I(\mathbf{r})$, (shown in Fig. 2(c), zoom in Fig. 2(h)) exhibits a regular fringe pattern with signal maxima occurring every 4 lines. To reconstruct the scattered field $U_S(\mathrm{r})$, we take the FT of the hologram, $\tilde{I}(\mathbf{q})$, (Fig. 2(d), zoom in Fig. 2(i)). We clearly see that the direct and conjugate terms, $A_R^* \tilde{U}_S$ and $A_R \tilde{U}_S^*$, have separated into the lower and upper halves of the FT plane, while the autocorrelation term *C* remains in the center of the FT. To isolate the direct term $A_R^* \tilde{U}_S$, we apply a window function (cosine window) to the FT as indicated by the dashed red box in Fig. 2(d). Shifting the result to the center of the FT plane and taking the inverse FT, we reconstruct the confocal amplitude and phase images, $A_S(\mathbf{r})$ and $\varphi_S(\mathbf{r})$.

#209297 - $15.00 USD Received 31 Mar 2014; revised 28 May 2014; accepted 31 May 2014; published 13 Jun 2014

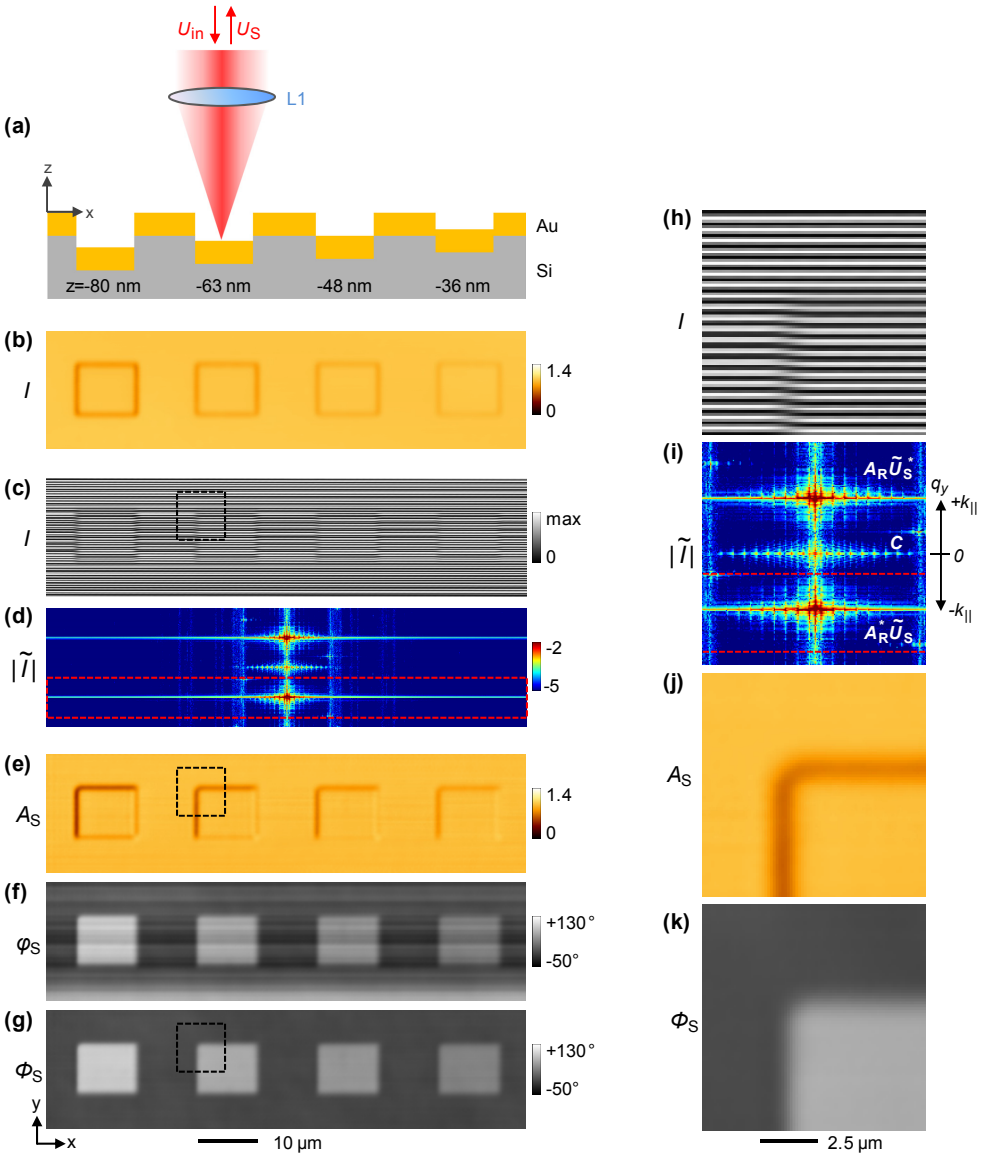

Fig. 2. Demonstration of SOH confocal microscopy with a test sample. (a) Schematic cross section of the test sample exhibiting pits of various depths (10 µm x 8 µm area, depth is indicated by the numbers below). (b) Non-interferometric confocal image. (c) Confocal synthetic hologram $I(\mathbf{r})$, (798 x 195 pixel, 80 µm x 20 µm, imaging time 195 sec, normalized to the intensity on the gold surface outside the holes). (d) Magnitude of Fourier-transform, $|\tilde{I}(\mathbf{q})|$, of $I(\mathbf{r})$ (logarithmic color scale). The red dashed line shows the width of the window function applied in the reconstruction process. (e) Reconstructed amplitude image $A_S(\mathbf{r})$. (f) Reconstructed phase image $\varphi_S(\mathbf{r})$. (g) Corrected phase image $\Phi_S(\mathbf{r})$. (h) Zoom into the region outlined by the dashed square in (c). (i) Zoom of center part of $|\tilde{I}(\mathbf{q})|$ showing the conjugate term $A_R\tilde{U}_S^*$, autocorrelation term C and the direct term $A_R^*\tilde{U}_S$ (from top to bottom). (j,k) Zooms into the regions outlined by the dashed squares in (e,g), showing the amplitude and corrected phase, $A_S(\mathbf{r})$ and $\Phi_S(\mathbf{r})$.

The confocal amplitude image $A_S(\mathbf{r})$ (Fig. 2(e)) shows a uniform contrast across the sample except at the pit walls, in agreement with the intensity image shown in Fig. 2(b). The

#209297 - $15.00 USD Received 31 Mar 2014; revised 28 May 2014; accepted 31 May 2014; published 13 Jun 2014

confocal phase image $\varphi_S(\mathbf{r})$ (Fig. 2(f)) reveals the pits as rectangular areas of a constant phase that scales with the depths of the pits: The deepest pit on the left shows the strongest phase shift with reference to the sample surface. Conversely, the shallowest pit on the right show the smallest phase shift, as expected.

Note that the phase image (Fig. 2(f)) exhibits phase drift in the y-direction, appearing as unexpected contrast changes between neighboring lines in form of horizontal stripes. We explain these artifacts by instabilities of the interferometer caused by air turbulences and thermal expansion, introducing changes of the phase difference between the scattered field $U_S(\mathrm{r})$ and the reference field $U_R(\mathrm{r})$. To remove the phase instabilities, we line-wise subtract an average value determined from data at the left and right end of each line, yielding a corrected phase image, $\Phi_S(\mathbf{r})$ (Fig. 2(g)). Indeed, both the sample surface and the bottom of the pits now appear with uniform phase, where we arbitrarily assigned a phase value of 0 to the sample surface.

In Fig. 3 we retrieve the surface profile of our test sample from the optical phase image by applying the following relation

$$h(\mathbf{r}) = \frac{\lambda}{2 \cdot 2\pi} \Phi_S(\mathbf{r}), \tag{4}$$

where $h(\mathbf{r})$ is the height with reference to the sample surface, $\Phi_S(\mathbf{r})$ is the corrected phase image and the extra factor of two accounts for the round-trip upon reflection from the surface. In Fig. 3(a) we plot the surface profile $h(\mathbf{r})$ of the pits shown in Fig. 2, and in Fig. 3(b) the surface profile of four further, shallower pits. We observe that all pits #1 to #8, exhibiting depths from 80 nm down to 4 nm, are clearly resolved. For comparison, we show AFM topography images of the pits #1 to #8 in Figs. 3(c) and 3(d) and extract line profiles across the pits, as indicated by the white arrows. Both the AFM images (Figs. 3(c) and 3(d)) and the optically obtained surface profiles (Figs. 3(a) and 3(b)) have been flattened by applying a 5th-order polynomial line leveling and the AFM images have been median filtered to remove isolated spikes caused by tip instabilities. We find good quantitative agreement between the AFM and the optically obtained topography, which can be appreciated by comparing the line profiles obtained from the optical image (red curves in Figs. 3(e) and 3(f)) with line profiles obtained from the AFM topography image (black curves in Figs. 3(e) and 3(f)). Particularly, both the pit width and pit depth are correctly resolved by SOH confocal microscopy. We note that the pit depth obtained from AFM topography is systematically 6% larger in comparison to the optically obtained topography, which we attribute to an error in the height calibration of the AFM.

Exemplarily, we show in Fig. 3(g) the line profiles for the pit #1 and pit #5. As can be seen at the pit walls, the lateral resolution in the optically-obtained surface profile (red line) is poorer than in the AFM topography (black line) because of diffraction. We estimate a lateral height resolution of about 0.54 μm for the optically obtained topography by measuring the distance in which the height $h(\mathbf{r})$ changes from 20% and 80% at the pit edges. This number is characteristic for our setup shown in Fig. 1, where a NA = 0.4 objective is employed and imaging is performed at a wavelength of λ = 632.8 nm. The lateral height resolution can easily be improved by using higher-NA objectives and illuminating at shorter wavelengths. To determine the vertical (depth) resolution, we show optical and AFM topography of pit #8 in Figs. 3(h) and 3(i), respectively. Both images visibly resolve the same height profile pattern, which exhibits randomly distributed areas of greater (dark color) and lower height (bright color) across the sample surface (e.g. at the region marked by the black arrow in Fig. 3(h)).

#209297 - $15.00 USD Received 31 Mar 2014; revised 28 May 2014; accepted 31 May 2014; published 13 Jun 2014

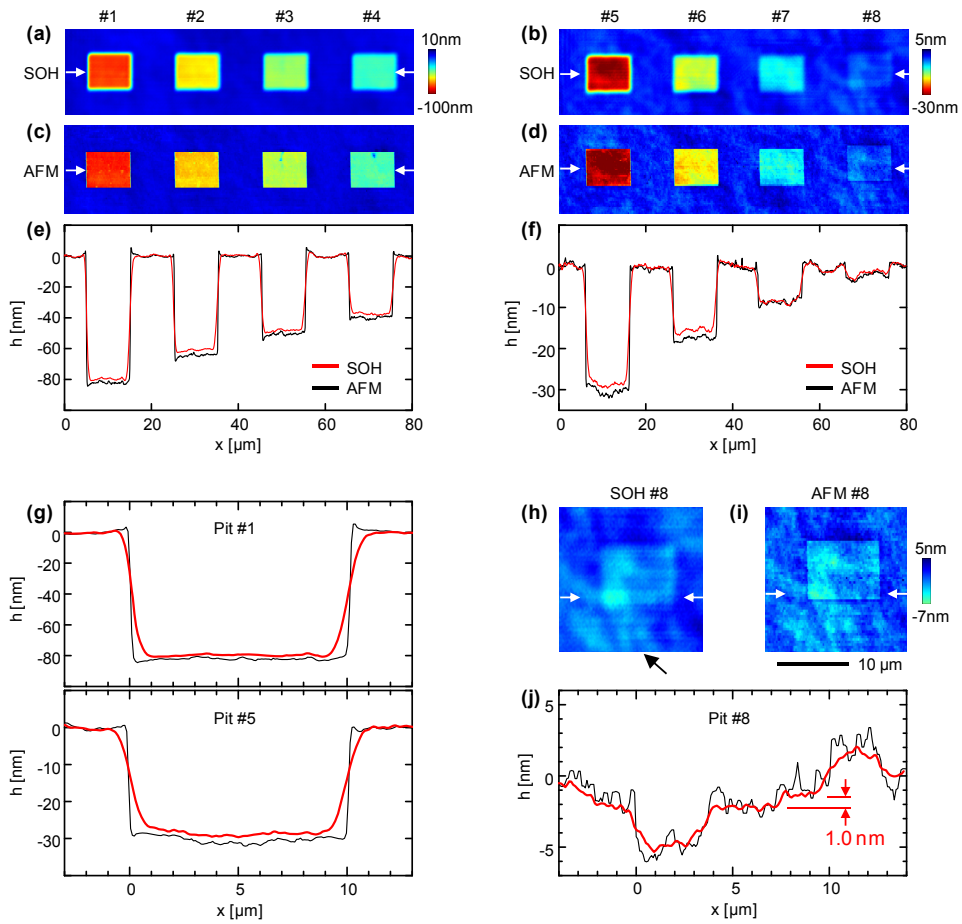

Fig. 3. Optically-obtained surface profile of the test sample. (a,b) Surface profiles obtained with SOH confocal microscopy, showings pits #1 to #4 and #5 to #8 (c,d) AFM topography images of pits #1 to #4 and #5 to #8. (e,f) Line profiles taken across the pits as indicated by the white arrows in (a-d). The optical line profiles (marked by 'SOH', red lines) represent data from a single line in (a,b), the AFM line profiles (black lines) represent the average over 10 neighboring lines in (c,d). (g) Zooms of the line profiles of pits #1 and #5 from (e) and (f), respectively. (h) Zoom of the optically obtained surface profile of pit #8 from (b). (i) Zoom of the AFM topography of pit #8 from (d). (j) Line profiles taken from (h,i) across pit #8 as indicated by the white arrows. The black arrow in (h) points to a region exhibiting thickness variations of the Au cladding that are resolved in the optically-obtained surface profile as well as in AFM topography (see text).

These patterns represent nanoscale variations of the Au film thickness, which are created during the deposition process (Argon sputtering). Interestingly, we resolve these thickness variations by applying an optical (non-contact) method. We quantify the surface profiles by extracting a line profile from Figs. 3(h) and 3(i), revealing that SOH confocal microscopy accurately reproduces the AFM topography (Fig. 3(j)). Particularly, a height step of only 1 nm (at position x = 7 µm) is clearly resolved in the optically obtained topography. From the region left (x = 4 to 7 µm) and right (x = 7 to 9 µm) to the height step, where we assume that the sample is flat, we estimate the optical vertical resolution to be 0.13 nm (RMS). Remarkably, such subnanometer-scale vertical resolution has been achieved with SOH implemented in a homebuilt confocal microscope setup, which has not been optimized for phase stability and vibration isolation. As major limiting factors in the stability of the optical phase and thus the accuracy in height resolution we identify (i) the stability of the Michelson

#209297 - $15.00 USD Received 31 Mar 2014; revised 28 May 2014; accepted 31 May 2014; published 13 Jun 2014

interferometer, (ii) the efficiency in shielding against external vibrations and air turbulences, (iii) the precision (noise) of the employed piezo stages for sample scanning and translation of the reference mirror. We expect that also detector noise could become a major limiting factor in case of low-power illumination or weak scattering from the sample, which will decrease the signal-to-noise ratio of the detector signal $I(\mathbf{r})$ and accordingly increase the noise in the phase signal $\varphi_S(\mathbf{r})$. Further studies are required to clarify the role of these limitations on the achievable depth resolution of SOH confocal microscopy, which however would go beyond the scope of this paper. We expect that optimization of the microscope setup, where these limitations are addressed and improved, could allow for resolving even single atomic layers. Recently, optical contrast has been observed at single atomic layers using a differential interference contrast microscope [17].

We conclude that SOH provides reliable quantitative phase imaging in confocal microscopy. While the achievable lateral resolution is diffraction-limited, SOH confocal microscopy could find use in metrology applications, where micrometer-scale lateral resolution is acceptable, but nanometer-scale depth resolution is required – with the additional benefit of being a non-contact profiling technique [5].

4. Surface profiling of an onion cell

In Fig. 4, we demonstrate an application of SOH confocal microscopy for biological microscopy by mapping the surface of a single onion cell [18–20]. To this end, a layer of onion cells is placed on a support (paper) without further preparation. Imaging is performed by focusing the illuminating beam on the top cell surface and detecting the reflected light (Fig. 4(a)). Figure 4(b) shows a conventional, non-interferometric image of the onion cell surface, which was acquired by blocking the reference beam. The image shows a section of the onion cell with the onion cell being aligned along the y-direction. Strong reflection intensity is observed at the center part while intensity falls off towards the side of the cell, which we attribute to the bulging of the onion cell and the point spread function of the microscope. More precisely, the cell surface moves out of the focal plane while scanning the sample at a fixed height (depth resolution of our confocal microscope is estimated to 1.2 μm) and the increasing slope of the surface towards the side causes reflection outside of the limited NA of the microscope objective.

Next, we applied SOH to obtain confocal amplitude and phase images of the onion cell surface. The confocal amplitude image, $A_S(\mathbf{r})$, (Fig. 4(c)) shows a similar contrast to the non-interferometric image (Fig. 4(b)). The confocal phase image, $\varphi_S(\mathbf{r})$, (Fig. 4(d)) shows strong phase wrapping in horizontal direction because of the 2π phase ambiguity. We manually unwrap the phase in the central region of the onion cell, where the phase is sufficiently well defined, and apply Eq. (4) to convert the phase into height information. The resulting surface profile $h(\mathbf{r})$ shows the curved shape of the onion cell (Fig. 4(e)), as can also be appreciated with the line profile taken horizontally across the cell (Fig. 4(g)). To display better the features on the onion cell surface, we apply a spatial high-pass filter to the data in Fig. 4(e), thus effectively removing most of the bulging of the cell surface, while preserving surface features. The filtered height image, $H(\mathbf{r})$, (Fig. 4(f)) reveals several pits and trenches on the surface with depths on the 100 nanometer scale and measuring several micrometer in width. While these features could already be recognized in the non-interferometric image by their dark and bright rims, however, the height image obtained from the confocal phase data provides the quantitative surface profile. Exemplarily we extract a horizontal line profile as indicated by the white dashed line, showing a step (mark ‘a’) with a height of 71 nm and a pit (mark ‘b’) with a depth of about 85 nm. Such information could provide valuable input for cell biology. We conclude that holographic quantitative phase mapping in confocal microscopy provides a non-contact technique for surface profiling with nanometer depth resolution, which could be attractive for studying biological samples even in vivo.

#209297 - $15.00 USD Received 31 Mar 2014; revised 28 May 2014; accepted 31 May 2014; published 13 Jun 2014

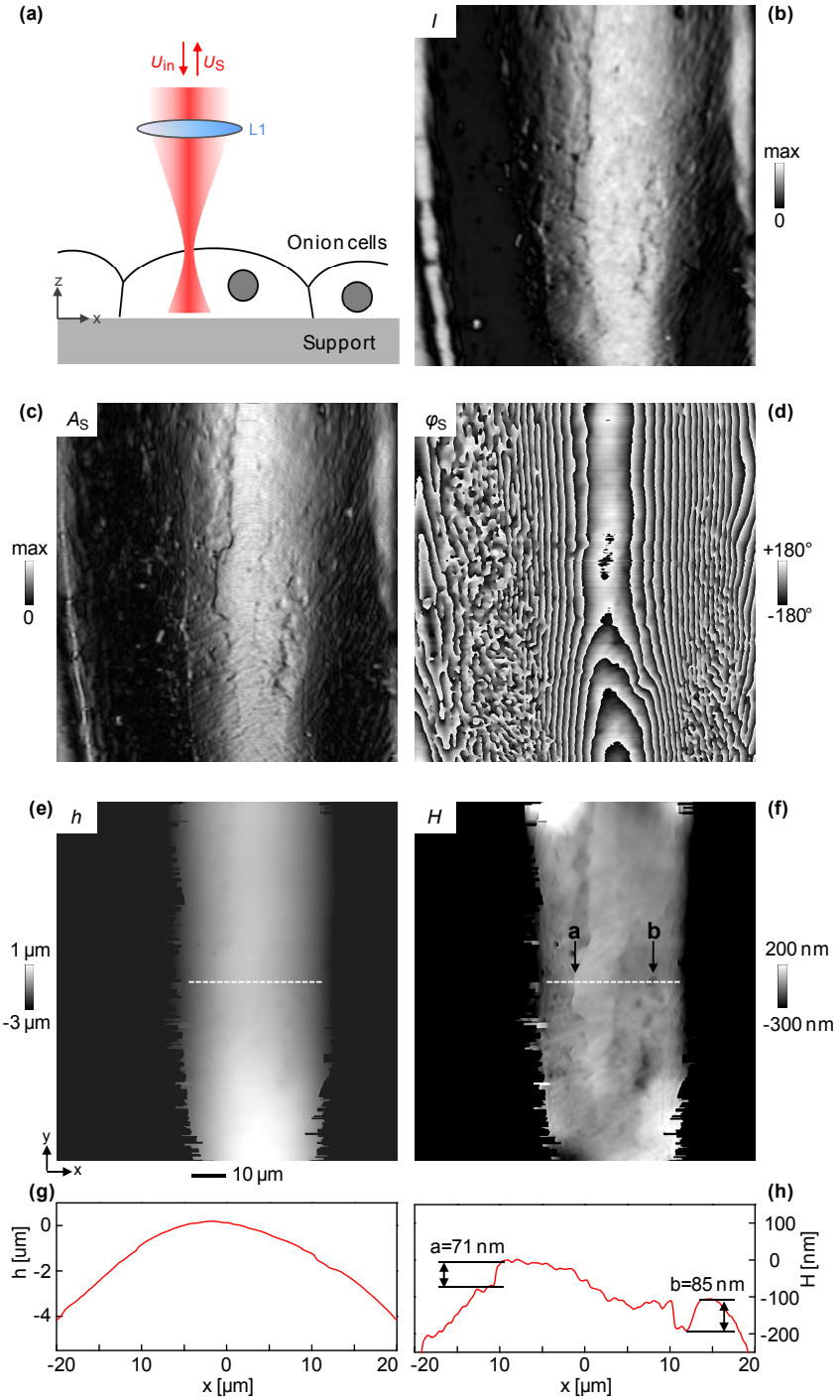

Fig. 4. Surface profiling of an onion cell. (a) Schematic. (b) Conventional, non-inteferometric confocal image of the surface of a single onion cell. The cell is aligned in y-direction and only part of the cell is shown with the cell walls visible at the left and right border. (c-d) Confocal amplitude and phase images, $A_s(\mathbf{r})$ and $\varphi_s(\mathbf{r})$, obtained with SOH (1500 x 1500 pixel, 100 µm x 100 µm, imaging time 25 min). (e) Surface profile of the onion cell $h(\mathbf{r})$. (f) High-pass filtered surface profile $H(\mathbf{r})$ to reveal details on the surface. (g,h) Line profiles taken along the dashed line in (e) and (f), respectively.

#209297 - $15.00 USD Received 31 Mar 2014; revised 28 May 2014; accepted 31 May 2014; published 13 Jun 2014

5. Discussion

The imaging speed in our SOH confocal microscope is limited by the sample scanning approach. The imaging time in Figs. 2 and 3 was 154 seconds and 1500 seconds in case of Fig. 4. While the imaging time has not been optimized in our homebuilt confocal microscope, a significant speed improvement can be expected when using a beam-scanning approach. Note that SOH in principle could be implemented in a beam-scanning confocal microscope, which will be subject of future research.

We note that SOH is a method that relies on spatial filtering and thus requires that the direct, autocorrelation and the conjugate terms separate in the FT space. Therefore, SOH requires some degree of oversampling in the slow scan direction as determined either by the inherent bandwidth of the sample or the bandwidth of the image passed by the optical system, whichever is smaller. Four times oversampling ensures that the direct, conjugate and auto correlation terms may be separated in the Fourier domain. If the reference is much stronger than the scattered field, as little as two-times oversampling may suffice.

6. Conclusions

We have demonstrated and verified synthetic optical holography (SOH) as a new method for quantitative phase imaging in confocal optical microscopy. The implementation of SOH in a confocal microscope was technically simple because only a linearly moving mirror needed to be added to the microscope setup without requiring any synchronization to the sample scanning. We applied confocal phase imaging to non-contact surface profiling of a test sample and achieved diffraction-limited lateral and sub-nanometer vertical resolution. We furthermore mapped the surface of an onion cell and revealed nanometer-scale height features on the cell surface. We remark that the current implementation of SOH has not been optimized for a compact design. We envision more compact implementations of SOH in existing confocal microscopes, for example, in form of Mirau interference objectives, where the sample or the objective is vertically translated while the sample is scanned. Such compact implementations could provide better phase stability and improved vertical resolution.

Beyond (bio)metrology applications, SOH could also be employed for phase-resolved confocal bio-imaging and second harmonic microscopy. In confocal fluorescence microscopy, for example, SOH could provide quantitative phase mapping of the Rayleigh-scattered light in addition to the detection of fluorescence emission, yielding surface profiles of cell surfaces with standard diffraction-limited lateral resolution, but with nanometer height resolution, even in vivo. SOH confocal microscopy could also be employed for stain-free and dye-free cellular imaging and neuroimaging [21,22], even in reflection [23].

Acknowledgments

This work was financially supported by the ERC Starting Grant No. 258461 (TERATOMO). M. J. P.-R. acknowledges the financial support from FEI Company (The Netherlands) within the framework of a collaborative project.

#209297 - $15.00 USD Received 31 Mar 2014; revised 28 May 2014; accepted 31 May 2014; published 13 Jun 2014